Estimation of superconducting cavity bandwidth and detuning using a Luenberger observer

Bozo Richter,[1,2,*] Andrea Bellandi,[3] Julien Branlard,[1]
Leon Speidel,[4] and Annika Eichler[1,2]

[1]*Deutsches Elektronen-Synchrotron DESY, Notkestraße 85, 22607, Hamburg, Germany*
[2]*Technische Universität Hamburg TUHH, Am Schwarzenberg-Campus 1, 22549, Hamburg, Germany*
[3]*Belgian Nuclear Research Centre SCK-CEN, Boeretang 200, 2400 Mol, Belgium*
[4]*Universität Hamburg UHH, Mittelweg 177, 22549, Hamburg, Germany*

(Received 15 July 2025; accepted 11 February 2026; published 8 May 2026)

Enabled by progress in superconducting technology, several continuous wave linear accelerators are foreseen in the next decade. For these machines, it is of crucial importance to track the main cavity parameters, such as the resonator bandwidth and detuning. The bandwidth yields information on the superconducting state of the cavity. The detuning should be minimized to limit the required power for operation of the cavity. The estimation of these parameters is commonly implemented in the digital electronics of the low-level rf control system to minimize the computation delay. In this proceedings paper, we present a way to compute the bandwidth and detuning using a Luenberger observer. In contrast to previous methods, the state observer yields estimations at the native control system sample rate without explicitly filtering the input signals. Additionally, the error convergence properties of the estimations can be controlled intuitively by adjusting gain parameters. Implementation considerations and test results for the derived observer are presented in the manuscript.

DOI: 10.1103/48zw-grdp

I. INTRODUCTION

The operation of future superconducting radio-frequency (SRF) linear particle accelerators, such as LCLS-II-HE [1,2], SHINE [3,4], and the European XFEL (EuXFEL) [5–7], relies heavily on advanced diagnostic and control methods. These methods are essential to maximize the availability and efficiency of accelerators, particularly when operating at high rf duty cycles with long pulses or in continuous wave (cw). Accurately estimating cavity detuning and bandwidth is a key requirement for achieving optimal performance in SRF particle accelerators.

Cavity detuning $\Delta\omega$ is the difference between the cavity resonance frequency ω_0 and the driving signal frequency ω, and should be minimized in order to reduce the accelerating system rf power consumption. Pressure drifts, ponderomotive instabilities, and microphonic effects can increase the magnitude of detuning [8].

The ratio of detuning to half bandwidth has a significant impact on power requirements. New cw facilities operate at low cavity half bandwidths in the range of tens of Hertz, i.e., comparable to magnitudes of detuning. Therefore, real-time controllers compensating the detuning are required [9], and they require accurate estimates of detuning for effective operation.

The cavity half bandwidth $\omega_{1/2}$ is inversely proportional to the quality factor of the rf cavity resonator system, including energy dissipation in the cavity itself and in externally coupled peripherals. Sudden dissipative processes such as quenches can be identified by observing the half bandwidth, increasing the operational safety and reducing potential cryogenic downtime.

In the past, there have been attempts to compute these parameters inside the field programmable gate array (FPGA) logic of low-level rf (LLRF) systems [10,11]. The major limitation of these methods is their dependence on explicit differentiation of the cavity rf probe signal. To limit the effect of noise on the estimation of the parameters, it is necessary to apply low-pass filters. However, the smoothing produced by the filtering process results in signal distortions at the boundaries of pulse transitions. Consequently, a compromise between noise reduction and pulse transition distortion must be made.

Recent work on cavity parameter identification proposed a recursive least squares (RLS)-based approach to estimate $\Delta\omega$ and $\omega_{1/2}$ based on first-order explicit Euler discretization of the cavity rf equation [12]. The algorithm identifies both

[*]Contact author: bozo.richter@desy.de

parameters independently and effectively behaves as a first-order low-pass filter on the corresponding true system parameters. New rf measurements are weighted by a continuously updating factor proportional to the empirical variance of the rf measurements, while previous parameter estimates decay aaccording to a constant forgetting factor. Because the RLS approach does not require filtering of measurements, it is not subject to the pulse-boundary problem.

In this paper, we present an alternative technique based on the Luenberger observer [13,14]. Although nonlinear stochastic filters [15,16] could offer more robust estimation, this linear deterministic state observer is selected to avoid the additional computational complexity of stochastic filters, e.g., noise covariance estimation, thereby reducing the FPGA implementation footprint and minimizing estimation latency. Compared to other SRF cavity parameter estimation techniques in the literature, the Luenberger observer also provides filtered estimations of the cavity accelerating gradient. The error dynamics of the component can be tuned by simply defining the desired parameter estimation bandwidth through observer pole placement.

In Sec. II, the rf cavity model is introduced. Section III is devoted to the derivation of the observer. In Sec. IV, the observer's estimation error is analyzed formally and in simulation, and Sec. V presents results from experimental data of SRF accelerating modules at EuXFEL facilities. Finally, the LO is compared to other algorithms in Sec. VI.

II. CAVITY MODEL

Superconducting cavity rf dynamics without beam loading are generally described by the state space model [17]

$$\frac{\mathrm{d}}{\mathrm{dt}}\begin{bmatrix} v_I \\ v_Q \end{bmatrix} = \begin{bmatrix} -\omega_{1/2} & -\Delta\omega \\ \Delta\omega & -\omega_{1/2} \end{bmatrix}\begin{bmatrix} v_I \\ v_Q \end{bmatrix} + 2\omega_{1/2}\begin{bmatrix} u_I \\ u_Q \end{bmatrix}. \quad (1)$$

Here, v_I and v_Q are the in-phase and quadrature components of the rf cavity probe signal, and u_I and u_Q are the in-phase and quadrature components of the rf cavity forward signal. In this paper, all quantities except the input coupling factor $2\omega_{1/2}$ are assumed to be time varying.

The cavity half bandwidth reflects dissipative events in the cavity walls by its relation to the cavity unloaded quality factor Q_0 and is defined as

$$\omega_{1/2} = \frac{\omega_0}{2Q_L} = \frac{\omega_0}{2Q_0} + \frac{\omega_0}{2Q_{\mathrm{ext}}}, \quad (2)$$

where Q_{ext} is the external and Q_L the loaded quality factor. During nominal operation of SRF cavities, $Q_0 \gg Q_{\mathrm{ext}}$ and

$$Q_L \simeq Q_{\mathrm{ext}} \Leftrightarrow \omega_{1/2} \simeq \omega_{1/2}^{\mathrm{ext}} = \frac{\omega_0}{2Q_{\mathrm{ext}}}. \quad (3)$$

When either Q_0 or Q_{ext} decreases, an increase in cavity bandwidth is observed, cf. Eq. (2). Changes in Q_{ext} are caused by coupler movement or heating with time constants of seconds up to hours, while anomalous dissipation events lead to significant changes in Q_0 within fractions of a second. Hence, the effects can be distinguished clearly.

Solving the cavity Eq. (1) for $\Delta\omega$ and $\omega_{1/2}$, here referred to as the inverse model, leads to the approach of [10,11]

$$\begin{aligned} \omega_{1/2} &= \frac{v_I(2\omega_{1/2}^{\mathrm{ext}} u_I - \dot{v_I}) + v_Q(2\omega_{1/2}^{\mathrm{ext}} u_Q - \dot{v_Q})}{v_{\mathrm{acc}}^2}, \\ \Delta\omega &= \frac{v_Q(2\omega_{1/2}^{\mathrm{ext}} u_I - \dot{v_I}) - v_I(2\omega_{1/2}^{\mathrm{ext}} u_Q - \dot{v_Q})}{v_{\mathrm{acc}}^2}, \end{aligned} \quad (4)$$

where the approximation of Eq. (3) is applied to the input coupling and $v_{\mathrm{acc}} = \sqrt{v_I^2 + v_Q^2}$ is the cavity accelerating voltage.

III. DERIVATION OF THE OBSERVER

A Luenberger observer makes use of a known linear time-invariant (LTI) state space model $\dot{\mathbf{x}} = A\mathbf{x} + B\mathbf{u}$ and $\mathbf{y} = C\mathbf{x}$ to extract system state information from measured system outputs. In the state space model, $\mathbf{x}$, $\mathbf{u}$, and $\mathbf{y}$ are the vectors of system states, inputs, and outputs, and A, B, and C are the system, input, and output matrices. If the system representation is minimal and observable, all states can be recovered by a Luenberger observer.

Parallel to the operation of the plant, the model is simulated using the same inputs as applied to the plant. The difference between measurements of plant outputs and simulated outputs is multiplied by an observer gain matrix L to correct the simulation model's internal states $\hat{\mathbf{x}}$. This completes the structure of a Luenberger observer, as shown in Fig. 1.

If the model describes the plant dynamics perfectly, the difference between the observer's state dynamics

$$\dot{\hat{\mathbf{x}}} = A\hat{\mathbf{x}} + B\mathbf{u} + L(\mathbf{C}\hat{\mathbf{x}} - \mathbf{y}) \quad (5)$$

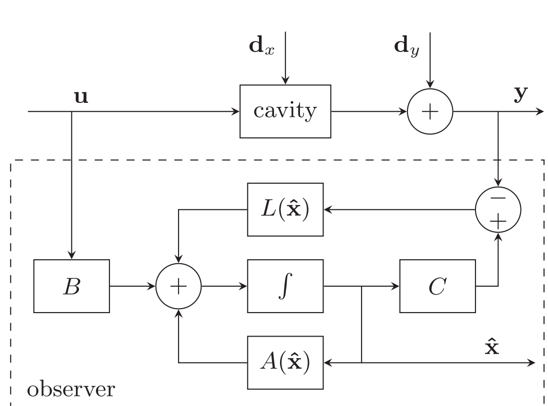

FIG. 1. Block diagram of the Luenberger observer.

and the model dynamics yields the estimation error dynamics

$$\dot{\mathbf{x}} - \dot{\hat{\mathbf{x}}} = \dot{\mathbf{e}} = (A + LC)\mathbf{e}. \tag{6}$$

These dynamics represent an autonomous system, as their states are independent of any input. By careful selection of the entries of L, the eigenvalues of $A + LC$ can be placed at values leading to desired error dynamics.

However, in the general cavity state space form of Eq. (1), the state vector contains neither $\Delta\omega$ nor $\omega_{1/2}$. Thus, the system representation is transformed assuming that significant variation in cavity half bandwidth occurs only by (partial) loss of superconductivity, i.e., greatly reduced Q_0. Hence, Eq. (2) is expressed as

$$\omega_{1/2}(t) = \omega_{1/2}^{\mathrm{ext}} + \Delta\omega_{1/2}(t), \tag{7}$$

collecting dynamic deviations of half bandwidth in the excess half bandwidth $\Delta\omega_{1/2}$. As in Eq. (4), the input coupling factor is assumed to be constant. Then, by definition of

$$V(\mathbf{x}) = \begin{bmatrix} -v_I & -v_Q \\ -v_Q & v_I \end{bmatrix} \qquad \mathbf{I} = \begin{bmatrix} 1 & 0 \\ 0 & 1 \end{bmatrix} \qquad \mathbf{0} = \begin{bmatrix} 0 & 0 \\ 0 & 0 \end{bmatrix} \tag{8}$$

and with Eq. (7), one can extend the state vector of Eq. (1) and reformulate the state space system to

$$\begin{aligned} \dot{\mathbf{x}} &= A(\mathbf{x})\mathbf{x} + B\mathbf{u} & \mathbf{y} &= C\mathbf{x} \\ \mathbf{x}^\top &= \begin{bmatrix} v_I & v_Q & \Delta\omega_{1/2} & \Delta\omega \end{bmatrix} & \mathbf{u}^\top &= \begin{bmatrix} u_I & u_Q \end{bmatrix} \\ A(\mathbf{x}) &= \begin{bmatrix} -\omega_{1/2}^{\mathrm{ext}}\mathbf{I} & V(\mathbf{x}) \\ \mathbf{0} & \mathbf{0} \end{bmatrix} & B &= 2\omega_{1/2}^{\mathrm{ext}} \begin{bmatrix} \mathbf{I} \\ \mathbf{0} \end{bmatrix} \\ C &= \begin{bmatrix} \mathbf{I} & \mathbf{0} \end{bmatrix}. \end{aligned} \tag{9}$$

In this formulation, the extended state vector $\mathbf{x}$ contains the excess half bandwidth $\Delta\omega_{1/2}$ and the detuning $\Delta\omega$, allowing to apply state estimation techniques to obtain real-time estimates of these parameters. However, as the system matrix A becomes dependent of elements of the state vector $\mathbf{x}$, Eq. (9) is not an LTI, but a quasilinear parameter varying (qLPV) state space model [18]. Variation of the external half bandwidth due to drifts in rf transmission line or coupler parameters is neglected throughout this work. Thus, the input and output matrices B and C are assumed to be constant.

A. Linear time-varying Luenberger observer

A Luenberger observer (LO) with time-varying gain matrix L is designed for the qLPV model given in Eq. (9). A block diagram of the LO is shown in Fig. 1. The design targets FPGA implementation at sampling rates in the MHz regime. Since mechanical and SRF cavity bandwidths are several orders of magnitude slower, Eq. (9) is treated as an LTI model with slowly drifting parameters. This avoids the complexity of a true LPV design at the cost of losing formal convergence guarantees and allows a straightforward design based on pole placement. The algebraic derivation of L is given in Appendix A.

All four eigenvalues of the estimation error dynamics in Eq. (6) are time invariant and equal to $p \in \mathbb{R}$ when applying the gain matrix

$$L(\mathbf{x}) = \begin{bmatrix} (2p + \omega_{1/2}^{\mathrm{ext}})\mathbf{I} \\ \frac{-p^2}{v_{\mathrm{acc}}^2} V(\mathbf{x}) \end{bmatrix}. \tag{10}$$

The magnitude of the time-varying entries is bounded by p^2/v_{acc}, since with $i \in \{1, 2\}$

$$\left| \frac{x_i}{v_{\mathrm{acc}}^2} \right| \leq \frac{1}{v_{\mathrm{acc}}}. \tag{11}$$

Hence, the time-varying adaption gains of $\Delta\omega_{1/2}$ and $\Delta\omega$ scale inversely proportional up to v_{acc}, and a necessary condition for application of the LO is $v_{\mathrm{acc}} > 0$. In application, this condition will technically hold due to rf pickup noise and offsets. To avoid accumulation of estimation error due to poor signal-to-noise ratio (SNR) of rfmeasurements, a minimum amplitude threshold for LO activation is proposed for implementation.

B. Discretization

For application in sampled data systems, exact discretization is used to obtain a discrete time representation of the cavity model, Eq. (9). Constant inputs are assumed between sampling instances k. A sampling instance k is related by the sampling time T to continuous time $t = kT$. The discretized system and input matrices Φ and Γ are given in block form by

$$\begin{aligned} \Phi_k(T) &= \begin{bmatrix} (1-\alpha)\mathbf{I} & \frac{\alpha}{w} V_k \\ \mathbf{0} & \mathbf{I} \end{bmatrix} & \Gamma(T) &= 2\alpha \begin{bmatrix} \mathbf{I} \\ \mathbf{0} \end{bmatrix} \\ V_k &= V(\mathbf{x}_k) & \alpha &= 1 - e^{-\omega_{1/2}^{\mathrm{ext}} T}, \end{aligned} \tag{12}$$

as shown in Appendix B.

For the discretized system, a state-dependent LO gain matrix Λ_k is designed, as in the continuous case. All four time-invariant eigenvalues of the estimation error dynamics are placed in $\rho \in \mathbb{R}$ by application of

$$\Lambda_k = \begin{bmatrix} (\alpha - 1 + 2\rho - 1)\mathbf{I} \\ -\frac{\mu}{v_{\mathrm{acc}}^2} V_k \end{bmatrix}, \tag{13}$$

where

$$\mu = -\frac{\omega_{1/2}^{\mathrm{ext}}}{\alpha}(\rho - 1)^2. \tag{14}$$

To obtain discrete time dynamics equivalent to continuous time poles in p, the eigenvalue mapping $\rho = e^{pT}$ can be applied. Restrictions in the choice of p and the derivation of Λ_k are given in Appendix C.

In the presented LO implementation, the estimation error decay bandwidth defined by the pole p remains as a free design parameter. Nevertheless, the external half bandwidth $\omega_{1/2}^{\mathrm{ext}}$ and an initial observer state vector $\mathbf{x}_0$ must be provided for application.

IV. ERROR ANALYSIS

To study the effects of process and output disturbances on the estimation error, two inputs $\mathbf{d}_x$ and $\mathbf{d}_y$ (see Fig. 1) are added to the qLPV cavity model, Eq. (9). A filter block

$$H(s) = \begin{bmatrix} \mathbf{I} & \mathbf{0} \\ \mathbf{0} & s\mathbf{I} \end{bmatrix} \tag{15}$$

is applied to $\mathbf{d}_x$ to make its bottom entries correspond to $\Delta\omega_{1/2}$ and $\Delta\omega$ of the true cavity system.

Given exact knowledge of the external half bandwidth and rf states to formulate the LO matrices, the continuous time estimation dynamics are

$$\dot{\hat{\mathbf{x}}} = A(\mathbf{x})\hat{\mathbf{x}} + B\mathbf{u} - L(\mathbf{x})(C\mathbf{e} + d_y) \tag{16}$$

leading to the error dynamics

$$\dot{\mathbf{e}} = (A(\mathbf{x}) + L(\mathbf{x})C)\mathbf{e} + H\mathbf{d}_x + L\mathbf{d}_y. \tag{17}$$

Application of the Laplace transformation and rearranging the equation yields the transfer matrices from the error driving terms $\mathbf{d}_x$ and $\mathbf{d}_y$ to the estimation error

$$\begin{aligned} G_{ed_x} &= (s\mathbf{I}_4 - A(\mathbf{x}) - L(\mathbf{x})C)^{-1}H \\ G_{ed_y} &= (s\mathbf{I}_4 - A(\mathbf{x}) - L(\mathbf{x})C)^{-1}L \end{aligned}, \tag{18}$$

where $\mathbf{I}_4$ is the 4×4 identity matrix. The tracking dynamics for half bandwidth and detuning can be characterized by the right block of the transfer matrix

$$[\mathbf{0} \quad \mathbf{I}](\mathbf{I}_4 - G_{ed_x}) = \frac{p^2}{(s-p)^2}\left[\frac{1}{v_{\mathrm{acc}}^2}V(\mathbf{x}) \quad \mathbf{I}\right]. \tag{19}$$

Consequently, the LO incorporates a decoupled pair of second-order low-pass filters acting on the true $\Delta\omega_{1/2}^{\mathrm{ext}}$ and $\Delta\omega$ of the cavity system, given an error-free setup of LO matrices.

The left block of Eq. (19) reveals that the parameter estimates are perturbed by process disturbances acting on v_I and v_Q, scaled by up to $|1/v_{\mathrm{acc}}|$. These rf process disturbances are also second-order low-pass filtered with bandwidth $|p|$ and have a nonzero static gain, thus they propagate to the estimates of $\Delta\omega_{1/2}$ and $\Delta\omega$ in steady state. They represent any input discrepancies between cavity and LO, e.g., input measurement errors, beam effects, or incorrectly chosen external half bandwidth.

The transfer characteristics of output measurement disturbances $\mathbf{d}_y$ to estimation errors of half bandwidth and detuning are given by

$$[\mathbf{0} \quad \mathbf{I}]G_{ed_y} = \frac{p^2(s + \omega_{1/2}^{\mathrm{ext}})}{(s-p)^2} \cdot \frac{1}{v_{\mathrm{acc}}^2}V(\mathbf{x}). \tag{20}$$

As the previously discussed rf disturbances in $\mathbf{d}_x$, these transfer functions have nonzero static gains, so static components in $\mathbf{d}_y$ lead to constant estimation errors in half bandwidth and detuning.

In application, the external half bandwidth is not known exactly, but an approximate value with an uncertainty factor $\kappa \approx 1$ in

$$\hat{\omega}_{1/2}^{\mathrm{ext}} = \kappa\omega_{1/2}^{\mathrm{ext}} \tag{21}$$

is used to set up the LO matrices $\hat{A}$, $\hat{B}$, and $\hat{L}$, applied in Eq. (16). To describe the effect on the estimates $\Delta\hat{\omega}_{1/2}$ and $\Delta\hat{\omega}$, the steady state solution of Eq. (16) using $\hat{A}$, $\hat{B}$, and $\hat{L}$ is compared to the steady state solution of Eq. (9) given the same input vector $\mathbf{u}$. For $\mathbf{d}_x = 0$ and $\mathbf{d}_y = 0$, one obtains the steady state estimates

$$\Delta\hat{\omega}_{1/2ss} = \kappa\Delta\omega_{1/2ss} \tag{22}$$

$$\Delta\hat{\omega}_{ss} = \kappa\Delta\omega_{ss}. \tag{23}$$

Evaluating Eq. (7) to obtain the estimated cavity half bandwidth

$$\hat{\omega}_{1/2ss} = \kappa(\omega_{1/2ss} + \Delta\omega_{1/2ss}) \tag{24}$$

reveals that both parameter estimates are scaled by κ.

Acceleration of a charged particle beam transfers energy from the cavity to the beam. This energy loss can be compensated by a counteracting increase in forward power to maintain the cavity in steady state. However, these beam effects are not included in the observer design, hence acting as a disturbance on the estimation. The corresponding apparent change in detuning and half bandwidth due to beam effects can be calculated as shown in Appendix D.

A. Nonlinear simulation

To validate the results of the simplified linear analysis, the discrete time LO is applied in an open-loop cavity simulation. Results are displayed in Fig. 2. The simulation is based on the continuous time nonlinear cavity dynamics, Eq. (1), evaluated by a fourth-order Runge-Kutta solver at a 9 MHz sampling rate. The detuning dynamics are simulated by a fifth-order filter excited by v_{acc}^2 and an additional free input representing a mechanical actuator.

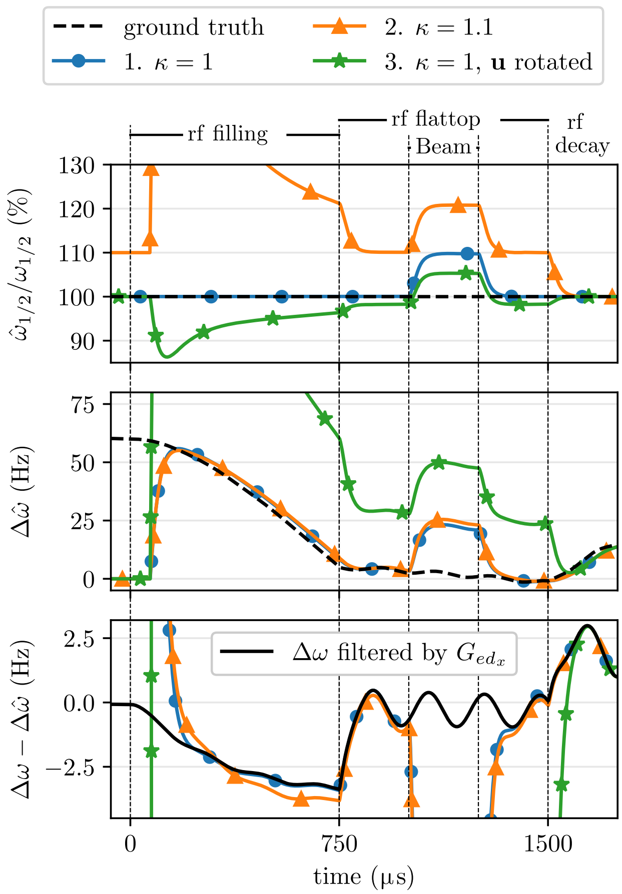

FIG. 2. Estimated half bandwidth (top), detuning (center), and detuning estimation error (bottom) of a simulated rf pulse with typical XFEL cavity parameters. Simulation state trajectories (dashed) are compared to LO estimations for ideal (filled circles) and mismatched (triangles) initial conditions, and a wrongly calibrated rf drive signal (stars).

The cavity parameters are based on EuXFEL specifications; however, the rf setpoint timing and scaling are adjusted to allow for clearer visualization. The external half bandwidth is set to 141 Hz, corresponding to $Q_L = 4.6 \times 10^6$ at a generator frequency of 1.3 GHz. The electromechanical coupling is $-1\ \mathrm{Hz/(MV)^2}$, and the simulated maximum v_{acc} is 8 MV.

Similar to operation at EuXFEL, the mechanical actuator excites the detuning dynamics with a sinusoidal stimulus about 6 ms prior to the rf drive pulse. The rf drive pulse is composed of two sections of constant drive power: First, high power is provided in a filling phase of 750 μs where the cavity field rises to its target value for acceleration. Then follows a 850 μs flattop, during which the drive power is set to maintain the cavity field. Finally, the drive is disabled, resulting in the field decay.

An artificial beam compensation term is superimposed on the simulated rf drive signal starting at 1000 μs and ending at 1250 μs. The apparent changes in half bandwidth and detuning are 14.1 Hz and 20°. The simulated cavity dynamics are not altered because the additional drive term is assumed to perfectly compensate for beam loading effects.

After simulation and drive signal modification, the rf signals are provided to the discrete time LO, which is set up with a pole frequency of 10 kHz. To avoid large gains during the filling phase in the bottom rows of Λ_k, $g_{2,k}$ is set to zero until $v_{\mathrm{acc}} > 1$ MV. The effects of initialization and calibration errors are investigated by setting the initial LO states to $\hat{\mathbf{x}}_0 = \mathbf{0}$ and furthermore (i) $\kappa = 1$, (ii) $\kappa = 1.1$, (iii) $\kappa = 1$, and $\mathbf{u}$ rotated by 10°.

Scenario 1 (-●-) shows a flat bandwidth estimation and tracks the detuning as expected, with constant offsets in the beam region. There, the expected apparent changes in estimated quantities are observed, exhibiting critical damping in the transitions. Except for the beam region, the detuning estimation error converges to the response of G_{dx} from Eq. (18), see bottom plot in Fig. 2.

Scenarios 2 (-▲-) and 3 (-★-) both show steady state bandwidth estimation errors with strongly damped transients at drive power changes. During rf filling, the half bandwidth estimation error decay is significantly slower than during the flattop, possibly due to neglecting derivatives of rf states during LO design.

The initial detuning estimation error decays equally fast in scenarios 1 and 2. In scenario 3, both bandwidth and detuning are subject to steady state estimation errors as long as drive power is supplied to the cavity. In all scenarios, both bandwidth and detuning estimation converge correctly during rf decay, given no static offsets in rf drive and cavity measurements.

Consequently, drive power calibration error and wrong external half bandwidth initialization are clearly recognizable in pulsed operation, where the forward power varies significantly and regularly. During cw operation, rf drive is supplied to the cavity persistently, and a free cavity response is not available. However, if the rf drive calibration is trusted, $\omega_{1/2}^{\mathrm{ext}}$ may be corrected by introducing rf drive variations and minimizing the resulting estimated half bandwidth deviation. Otherwise, techniques such as [19] may be required to verify the external half bandwidth and correct signal calibration, or cw operation is interrupted for calibration and computation of $\hat{\omega}_{1/2}^{\mathrm{ext}}$.

V. EXPERIMENTAL RESULTS

The presented discrete time LO is applied to nominal and anomalous experimental data obtained from EuXFEL and the cryo module test bench (CMTB). At both facilities, the same type of cryomodule with SRF TESLA cavities is installed, but driven in different operating modes.

The data used is chosen to showcase the LO's ability to indicate occurrence of quenches and distinguish them from nominal pulses. Code and data used are provided in [20] and [21].

A. Short pulse

The EuXFEL is a user facility driven by a linear accelerator, yielding an electron beam with energies up to 17.5 GeV. The high energy electron beam is used to generate ultra short x-ray flashes with photon energies up to 25 keV to enable photon science experiments. The accelerator is operated in pulsed mode at a 10 Hz repetition rate with 1.4% rf duty factor, called short-pulse mode. Each rf station consists of four cryomodules and a total of 32 cavities. All cavities are driven in parallel by a single klystron under vector-sum control.

Front end CPUs have access to rf data traces with a length of 2^{14} samples obtained at a rate of 9 mHz, yielding a covered time span of 1.8 ms per pulse. On occurrence of a quench, an archiving system stores decimated data at 1 mHz for postmortem analysis, including 200 pulses prior to and 50 more pulses beginning with the anomaly. One of these datasets is used for application of the LO. The recorded data is preprocessed by applying the energy based crosstalk removal and signal calibration method to the first 100 pulses as presented in [22,23].

In Fig. 3, estimations obtained from the last nominal and the subsequent quenching pulse are shown as solid lines. A band of ± 6 standard deviations σ of all 200 nominal pulses estimates gives an indication of the error bars. The observer poles are placed at 10 kHz. Half bandwidth and detuning estimation are inhibited at acceleration voltages below 1 MV. The flattop acceleration voltage is 21 MV. During filling, the increasing rf measurement SNR leads to reducing noise and thus shrinking error bars in both estimated parameters. The critically damped low-pass characteristic of the estimation error is clearly recognizable at the beam induced apparent bandwidth change. Within the beam region, a quench is clearly visible by the sudden increase in excess bandwidth, clearly surpassing the 6σ band of nominal estimates. Given a corresponding decision metric for quench detection, protective reactions within the quenching pulse are possible.

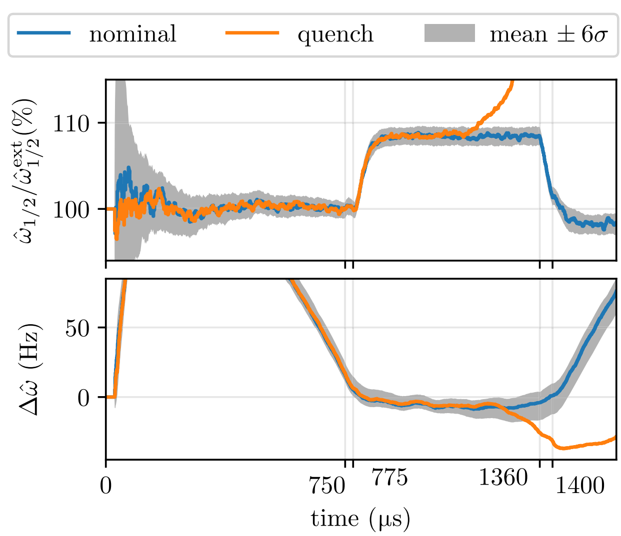

FIG. 3. Relative half bandwidth (top) and detuning (bottom) estimations of a nominal EuXFEL pulse with on-crest beam, and during a quench. The shaded areas mark the band of $\pm 6\sigma$ around the nominal mean estimate.

B. Continuous wave

CMTB is a test facility that can host one EuXFEL-type cryomodule with eight cavities. It is equipped with distinct LLRF systems for generator driven vector-sum and single cavity control, and self-excited loop (SEL) operation. An inductive output tube provides rf drive power of up to 40 kW to a waveguide distribution system connecting all eight cavities. This amplifier can be operated at any duty factor, including continuous wave. At CMTB, no electron beam is available.

The front-end CPU allows configurable data acquisition sample rates by decimating the available 9 MHz sample stream of the digital signal processor (DSP). In cw operation, data are acquired at 16.4 kHz, greatly reducing feasible estimation bandwidths. An experiment is conducted using a single cavity digital SEL controller with an output amplitude limiter. The amplitude limit is increased successively, until a quench occurs at a cavity probe voltage of 18 MV.

In Fig. 4, the relative changes of v_{acc}, $|\mathbf{u}|$ and the estimated half bandwidth of an LO with poles at 3 kHz are displayed. Again, a band of $\pm 6\sigma$ is shown around the nominal means of the LO bandwidth estimate and rf probe amplitude. Starting at 50 ms, the time scale is stretched by a factor of 20. The drive power remains close to an arbitrary nominal value at all times. Indicating a quench, the cavity probe voltage decays starting at 50.7 ms, and the estimated half bandwidth increases.

In the presented case, the quench is clearly visible from the cavity voltage alone. However, setpoint tracking controllers, detuning and beam loading pose additional challenges when implementing a reliable quench detector based on direct interpretation of rf trajectories. In contrast, the LO

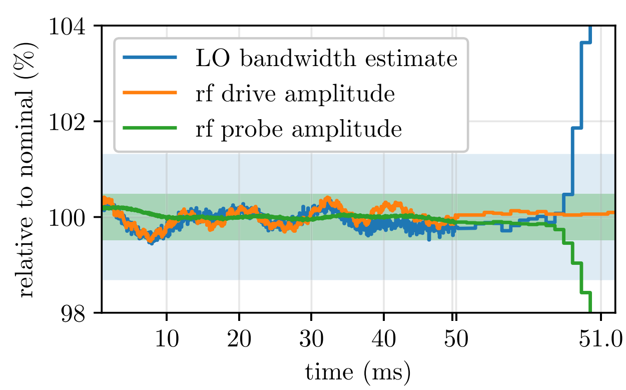

FIG. 4. Normalized bandwidth estimation and cavity voltage measurements of cw quench test in SEL at CMTB.

yields an explicit estimate of the external half bandwidth in any case.

VI. COMPARISON

The LO is compared with and benchmarked against the approach of inverting the cavity equations [10] and the RLS identification algorithm [12] on the experimental EuXFEL data used in Fig. 3.

Under idealized assumptions, the LO behaves as a second-order low-pass filter acting on the true system parameters, and the RLS approach as a first-order low-pass filter. Hence, clear expectations arise towards their performance. If the LO poles p are chosen to match that of the RLS filter, the RLS estimates will have a shorter rise time but also be noisier due to the higher filter gain above the bandwidth. However, a combination of RLS and a low-pass filter can reproduce any LO pole combination, as long as LO poles remain real. Nevertheless, the LO allows placement of complex-conjugate pole pairs (see Appendixes A and C), allowing the creation of second-order Butterworth filters. Hence, the rise time is improved while noise suppression is maintained.

The inverse model approach is not a filter in itself, as it is a stateless algorithm. However, it requires filtering of rf signals to denoise the rf state derivatives. The inverse model approach leads to similar estimates as the LO when using a second-order filter with equivalent poles, and similar estimates as RLS when using a first-order filter. However, rf filtering distorts transitions both from filling to flattop and from flattop to decay.

The LO therefore provides the freedom of selecting complex-conjugate pole pairs in contrast to RLS and avoids the pulse transition distortions present in the inverse model approach.

LO, RLS, and the inverse model approach are applied to the EuXFEL short-pulse dataset. All methods are setup with stable poles at 10 kHz. The LO and inverse model rf filter are configured as second-order Butterworth filters, the derivatives for the inverse model approach are then obtained by backward differences.

Figure 5 shows the means, Fig. 6 the standard deviations of estimates over the 200 nominal pulses using the discussed techniques. All approaches yield similar mean trajectories. Differences emerge in noise and speed of response, with the RLS estimates being faster but noisier. Both effects are expected due to the first- order filter behavior and therefore stronger high frequency signal content. In the transition from filling to flattop, the rf filtering used for the inverse model leads to undershoot in the bandwidth estimate and subsequent overshoot when the beam arrives. The detuning estimate seems unaffected. Remarkably, the bandwidth estimate of all approaches suffer from distortions in the pulse transition from filling to flattop, but the LO is least affected.

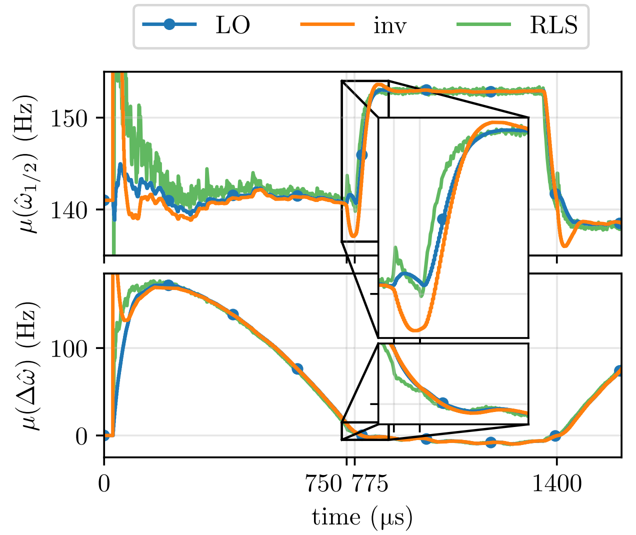

FIG. 5. Means $\mu(\cdot)$ of estimated half bandwidth $\hat{\omega}_{1/2}$ (top) and detuning $\Delta\hat{\omega}$ (bottom) from EuXFEL short-pulse data using different parameter estimation techniques.

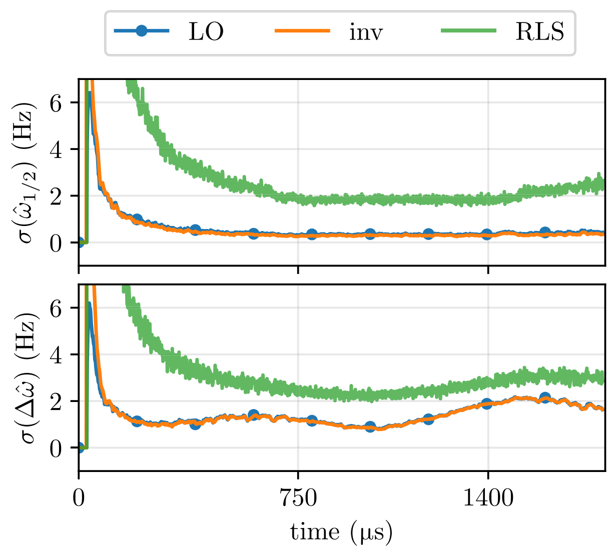

FIG. 6. Standard deviations $\sigma(\cdot)$ of estimated half bandwidth $\hat{\omega}_{1/2}$ (top) and detuning $\Delta\hat{\omega}$ (bottom) evaluated over 200 nominal EuXFEL rf pulses.

VII. CONCLUSION

An observer has been developed incorporating the non-linear coupling of detuning and rf cavity states, producing second-order filtered time series of the cavity system detuning and half bandwidth. The method relies on accurately calibrated, offset-free rf signals and precise estimates of the cavity half bandwidth.

The presented observer design respects the cavity system's inherent nonlinearity and offers a straightforward setup, requiring only intuitive tuning and initial parameters. Application on recorded experimental data is promising.

A real-time implementation operating at the native DSP sample rate remains to be tested. Compared to existing approaches, the LO allows error dynamics with complex-conjugate pole pairs and reduces distortions in pulse transitions.

Future efforts will include quench detection based on LO estimates and a detuning-aware feedback and feedforward rf controller, enabled by the low-delay, native-speed detuning estimation. Resonance control using downsampled detuning data is also anticipated. Further exploration may include a formal LPV stability analysis, advanced stochastic observer design, SNR evaluation at $\omega_{1/2}^{\mathrm{ext}} < 65$ Hz, beam parameter estimation, cw calibration, and online identification of the external half bandwidth.

ACKNOWLEDGMENTS

This work was partially funded in the context of the R&D program of the European XFEL. This project has received funding from the European Unions Horizon Europe research and innovation program under Grant Agreement No. 101131435.

DATA AVAILABILITY

The data that support the findings of this article are openly available [20,21].

APPENDIX A: OBSERVER POLE PLACEMENT

Derivatives of the rf states are neglected to allow for a straightforward observer design. In the following, an observer gain

$$L(x) = \begin{bmatrix} (\omega_{1/2}^{\mathrm{ext}} + \gamma)\mathbf{I} \\ W \end{bmatrix} \tag{A1}$$

will be designed, leading to the estimation error dynamics matrix

$$A_{\mathrm{cl}}(x) = A(x) + L(x)C = \begin{bmatrix} \gamma\mathbf{I} & V \\ W & 0 \end{bmatrix}. \tag{A2}$$

The chosen structure of L reduces the number of free design parameters to three and allows straightforward pole placement. Therefore, the eigenvalues of A_{cl} must be calculated. The characteristic polynomial

$$\det(\lambda\mathbf{I}_4 - A_{\mathrm{cl}}) = \det\left(\begin{bmatrix} (\lambda-\gamma)\mathbf{I} & -V \\ -W & \lambda\mathbf{I} \end{bmatrix}\right) \tag{A3}$$

is simplified using the Schur complement

$$\begin{bmatrix} A & B \\ C & D \end{bmatrix} = \begin{bmatrix} A - BD^{-1}C & B \\ 0 & D \end{bmatrix} \tag{A4}$$

revealing that

$$\begin{aligned} \det(\lambda\mathbf{I}_4 - A_{\mathrm{cl}}) &= \det\left[(\lambda-\gamma)\mathbf{I} - \frac{1}{\lambda}VW\right]\det(\lambda\mathbf{I}) \\ &= \det[(\lambda^2 - \lambda\gamma)\mathbf{I} - VW] \\ &= \det(\mu\mathbf{I} - VW) \end{aligned} \tag{A5}$$

is the characteristic polynomial of VW in μ, requiring $\lambda \neq 0$. Assuming that $v_{\mathrm{acc}}^2 = v_I^2 + v_Q^2 > 0$, the static eigenvalues μ_i can be assigned by setting

$$W = MV^{-1} = \begin{bmatrix} \mu_1 & 0 \\ 0 & \mu_2 \end{bmatrix} V^{-1} = \frac{1}{v_{\mathrm{acc}}^2}\begin{bmatrix} \mu_1 & 0 \\ 0 & \mu_2 \end{bmatrix} V \tag{A6}$$

as V is a scaled involution. Hence, $VW = VMV^{-1}$ is a similarity transformation of M and thus preserves the eigenvalues μ_i. The roots of Eq. (A5) are found by solving

$$0 = \lambda^2 - \lambda\gamma - \mu_i \tag{A7}$$

$$\Rightarrow \lambda_j = \frac{\gamma}{2} \pm \sqrt{\frac{\gamma^2}{4} + \mu_i}, \tag{A8}$$

with $i \in \{1, 2\}$ and $j \in \{1, 2, 3, 4\}$.

For a more intuitive observer tuning, one can introduce the pole location p and additional tuning parameters $f_i \in \mathbb{R}$ and set

$$\begin{aligned} \gamma &= 2p \\ \mu_i &= -f_i p^2 \\ \Rightarrow \lambda_j &= p(1 \pm \sqrt{1 - f_j}). \end{aligned} \tag{A9}$$

With $f_i = 1$, all $\lambda_j = p$, so the observer's estimation error dynamics are critically damped. The choice of W allows association of f_1 and f_2 to the speed of estimation of $\Delta\omega_{1/2}$ and $\Delta\omega$, respectively. For stable observer dynamics, one has to select $p < 0$ and $f_i > 0$ and ensure that $v_{\mathrm{acc}}^2 > 0$. For maximally flat filtering (Butterworth), set $f_i = 2$.

Then, the parameter varying observer gain providing time-invariant observer dynamics while neglecting parameter derivatives is

$$L(x) = \begin{bmatrix} \omega_{1/2}^{\mathrm{ext}} + 2p & 0 \\ 0 & \omega_{1/2}^{\mathrm{ext}} + 2p \\ \frac{f_1 p^2 v_I}{v_{\mathrm{acc}}^2} & \frac{f_1 p^2 v_Q}{v_{\mathrm{acc}}^2} \\ \frac{f_2 p^2 v_Q}{v_{\mathrm{acc}}^2} & \frac{-f_2 p^2 v_I}{v_{\mathrm{acc}}^2} \end{bmatrix} \tag{A10}$$

APPENDIX B: DISCRETIZATION

For verification in simulation and experimental validation, the developed continuous model is discretized using a zero-order hold with constant inputs between sampling instances.

By exploiting the matrix exponential and by defining

$$\bar{A}_w := -\frac{1}{w}A = \begin{bmatrix} \mathbf{I} & -\frac{1}{w}V \\ 0 & 0 \end{bmatrix} \tag{B1}$$

$$\Rightarrow \ \forall\, n \in \mathbb{N}\backslash\{0\}:\ A^n = (-w)^n \bar{A}_w, \tag{B2}$$

where $w := \omega_{1/2}^{\mathrm{ext}}$ to improve readability, one obtains the discrete time system matrix

$$\Phi(T) = e^{AT} = \sum_{k=0}^{\infty} \frac{T^k}{k!} A^k = \begin{bmatrix} \mathbf{I} & 0 \\ 0 & \mathbf{I} \end{bmatrix} + \bar{A}_w \sum_{k=1}^{\infty} \frac{(-wT)^k}{k!} \tag{B3}$$

$$= \begin{bmatrix} \mathbf{I}e^{-wT} & -\frac{1}{w}V(e^{-wT}-1) \\ 0 & \mathbf{I} \end{bmatrix}. \tag{B4}$$

The discrete time input matrix is

$$\Gamma(T) = \int_0^T e^{A\tau} B \,\mathrm{d}\tau = \begin{bmatrix} 2\mathbf{I}(1-e^{-wT}) \\ 0 \end{bmatrix}. \tag{B5}$$

By introducing $\alpha = 1 - e^{-wT}$,

$$\Phi(T) = \begin{bmatrix} (1-\alpha)\mathbf{I} & \frac{\alpha}{w}V \\ 0 & \mathbf{I} \end{bmatrix} \tag{B6}$$

$$\Gamma(T) = 2\alpha \begin{bmatrix} \mathbf{I} \\ 0 \end{bmatrix}. \tag{B7}$$

APPENDIX C: DISCRETE TIME POLE PLACEMENT

Analogous to the continuous case, the discrete time observer gain

$$\Lambda_k = \begin{bmatrix} (\alpha - 1 + \beta)\mathbf{I} \\ W_k \end{bmatrix} \tag{C1}$$

is designed using W as given in Eq. (A6). The closed-loop dynamic system matrix

$$\Phi_{k,\mathrm{cl}} = \Phi_k + \Lambda_k C = \begin{bmatrix} \beta\mathbf{I} & \frac{\alpha}{w}V_k \\ W_k & \mathbf{I} \end{bmatrix} \tag{C2}$$

and its characteristic polynomial

$$\det(\lambda \mathbf{I}_4 - \Phi_{\mathrm{cl}}) = \frac{\alpha^2}{w^2} \det\left((\lambda-\beta)(\lambda-1)\frac{w}{\alpha}\mathbf{I} - VW\right), \tag{C3}$$

where $\lambda \neq 1$, lead to closed-loop eigenvalues

$$\lambda_j = \frac{\beta+1}{2} \pm \sqrt{\frac{(\beta+1)^2}{4} - \beta + \frac{\alpha}{w}\mu_i} \tag{C4}$$

$$\text{where} \quad \mu_i = \frac{w}{\alpha}(\lambda-\beta)(\lambda-1) \tag{C5}$$

and again $i \in \{1,2\}$ and $j \in \{1,2,3,4\}$.

Introducing the continuous to discrete time eigenvalue mapping $\rho = e^{pT}$, tuning factors $\varphi_i \in \mathbb{R}$, and setting

$$\begin{aligned} \beta &= 2\rho - 1 \\ \mu_i &= \varphi_i \frac{w}{\alpha}(\beta - \rho^2) = -\varphi_i \frac{w}{\alpha}(1-\rho)^2 \end{aligned} \tag{C6}$$

leads to the discrete time eigenvalues

$$\lambda_j = \rho \pm (1-\rho)\sqrt{1-\varphi_i}, \tag{C7}$$

with the same tuning mechanism as the continuous eigenvalues in Eq. (A9).

Again, with both $\varphi_i = 1$ all four $\lambda_j = \rho = e^{pT}$, i.e., the observers estimation error dynamics are critically damped if $p < 0$. Also, the choice of W allows association of φ_1 and φ_2 to the speed of estimation of $\Delta\omega_{1/2}$ and $\Delta\omega$, respectively. Due to the discrete time eigenvalue mapping, $\varphi > 1$ does not increase the observer bandwidth if $\rho < 0.35$. For stable error dynamics, one has to ensure that $v_{\mathrm{acc}}^2 > 0$ and λ_j must remain strictly inside the unit circle. To fulfill the Nyquist criterion, one must select a p according to

$$-\frac{\pi}{T} < p < -\kappa w < 0, \tag{C8}$$

where $\kappa > 1$ is an arbitrary minimum continuous time pole relation factor. For $\varphi_i > 1$, one obtains complex conjugated discrete time poles. For the eigenvalues to remain inside the unit circle, φ_i must satisfy

$$\varphi_i < \frac{2}{1-\rho}. \tag{C9}$$

For $\varphi_i < 1$, one obtains two discrete time poles on the real axis. The pole farther left in the z plane is not problematic due to positivity of the exponential function, and the upper bound on p in Eq. (C8) implies

$$\varphi_i > 1 - \left(\frac{e^{-\kappa wT} - \rho}{1-\rho}\right)^2 \tag{C10}$$

hence

$$\max\left(1 - \left(\frac{e^{-\kappa wT} - \rho}{1-\rho}\right)^2, 0\right) < \varphi_i < \frac{2}{1-\rho}. \tag{C11}$$

Then, the parameter varying observer gain providing time-invariant observer dynamics while neglecting parameter derivatives is

$$\Lambda(x) = \begin{bmatrix} \alpha - 2 + 2\rho & 0 \\ 0 & \alpha - 2 + 2\rho \\ -\mu_1 \frac{v_I}{v_{\mathrm{acc}}^2} & -\mu_1 \frac{v_Q}{v_{\mathrm{acc}}^2} \\ -\mu_2 \frac{v_Q}{v_{\mathrm{acc}}^2} & \mu_2 \frac{v_I}{v_{\mathrm{acc}}^2} \end{bmatrix}. \tag{C12}$$

Again, $\varphi > 1$ exist to obtain a maximally flat filter response in the sense of Butterworth, but a closed expression is not known. A numerical approach is implemented in [20]. A simple approximation suitable for $\rho > 0.35$ is given by $\varphi \approx 0.33\rho + 1.11$.

The tuning factors f_i and φ_i introduced above can be used to move a pole pair away from p or ρ by the same Euclidean distance in opposite directions, either vertically for values above one, or horizontally for values below. However, changes in f_i and φ_i are not equivalent, since the map $\rho = e^{pT}$ is nonlinear.

Equivalent expressions can be found iff $f \coloneqq f_1 = f_2$ and thus $\varphi \coloneqq \varphi_1 = \varphi_2$. For given p, f, and T, the corresponding discrete time poles are obtained by setting

$$\rho = e^{pT} \cos(pT\sqrt{f-1})\varphi = 1 - \tan^2(pT\sqrt{f-1}). \tag{C13}$$

APPENDIX D: BEAM ESTIMATION

When operating with an off-crest beam, the estimated detuning represents the frequency offset from the detuning that minimizes the required forward power. Accordingly, the estimated bandwidth deviation reflects the amount of energy transferred to or extracted from the cavity by the beam. If the beam induced generator term is known, it can be subtracted from the measured forward signal before being fed into the NLO. Thus, the beam becomes transparent to the NLO, and the estimations remain unpertubed. For quench detection purposes, the transparent approach is preferable, whereas beam perturbed estimation is advantageous to track an energy optimal cavity tune. In the following, the effects of the latter approach on the estimated quantities are analyzed.

A steady state complex rf drive u_{ss} leading to the steady state complex rf cavity voltage v_{ss} without beam is described by inserting Eqs. (3) and (7) into Eq. (1), such that

$$2u_{\mathrm{ss}} = (1 + z_{\mathrm{ss}} + jy_{\mathrm{ss}})v_{\mathrm{ss}} \tag{D1}$$

after converting to complex notation with the complex unit j. Here, $z_{\mathrm{ss}} = \Delta\omega_{1/2}/\omega_{1/2}^{\mathrm{ext}}$ and $y_{\mathrm{ss}} = \Delta\omega/\omega_{1/2}^{\mathrm{ext}}$ are the apparent half bandwidth deviation and detuning, respectively.

Assume an additional complex rf drive term u_b compensates beam loading effects to maintain an accelerating voltage of v_{ss}. Then, the apparent half bandwidth deviation and detuning must be adjusted to fulfill Eq. (D1), leading to

$$2(u_{\mathrm{ss}} + u_b) = (1 + (z_{\mathrm{ss}} + z_b) + j(y_{\mathrm{ss}} + y_b))v_{\mathrm{ss}} \tag{D2}$$

where z_b and z_b are beam induced changes in apparent parameters, and thus

$$2u_b = (z_b + jy_b)v_{\mathrm{ss}}. \tag{D3}$$

The complex beam loading compensation voltage u_b maintaining an accelerating gradient of v_{acc} therefore induces a change in apparent half bandwidth and detuning of

$$\begin{aligned} \Delta\omega_{1/2,b} &= \omega_{1/2}^{\mathrm{ext}} z_b = 2\omega_{1/2}^{\mathrm{ext}} \mathrm{Re}\left(\frac{u_b}{v_{\mathrm{ss}}}\right) \\ \Delta\omega_b &= \omega_{1/2}^{\mathrm{ext}} y_b = 2\omega_{1/2}^{\mathrm{ext}} \mathrm{Im}\left(\frac{u_b}{v_{\mathrm{ss}}}\right). \end{aligned} \tag{D4}$$

[1] J. N. Galayda, The LCLS-II: A high power upgrade to the LCLS, in *Proceedings of the 9th International Particle Accelerator Conference (IPAC'18)* (JACoW, Geneva, Switzerland, 2018), pp. 18–23, 10.18429/JACoW-IPAC2018-MOYGB2.

[2] T. Raubenheimer, The LCLS-II-HE, a high energy upgrade of the LCLS-II, in *Proceedings of the 60th ICFA Advanced Beam Dynamics Workshop on Future Light Sources* (JACoW, Geneva, Switzerland, 2018), pp. 6–11.

[3] N. Huang, H. Deng, B. Liu, D. Wang, and Z. Zhao, Features and futures of x-ray free-electron lasers, Innovation **2**, 100097 (2021).

[4] B. Liu, D. Wang, L. Yin, and Z. Zhao, Progress of Shanghai HIgh repetitioN rate XFEL and extreme light facility (SHINE), in *Proceedings of the LINAC'22, Liverpool, UK* (unpublished).

[5] J. Sekutowicz, V. Ayvazyan, M. Barlak, J. Branlard, W. Cichalewski, W. Grabowski, D. Kostin, J. Lorkiewicz, W. Merz, R. Nietubyc, R. Onken, A. Piotrowski, K. Przygoda, E. Schneidmiller, and M. Yurkov, Research and development towards duty factor upgrade of the European X-ray Free Electron Laser linac, Phys. Rev. ST Accel. Beams **18**, 050701 (2015).

[6] E. Vogel, S. Barbanotti, A. Brinkmann, T. Buettner, J. Iversen, K. Jensch, D. Klinke, D. Kostin, W.-D. Möller, A. Muhs *et al.*, Status of the all superconducting gun cavity at DESY, in *Proceedings of the 19th International Conference on RF Superconductivity, Dresden, Germany* (JACoW, Geneva, Switzerland, 2019), Vol. 30, pp. 1087–1090.

[7] E. Gjonaj and D. Bazyl, Beam dynamics study of a cw L-band SRF gun for the high duty cycle EuXFEL, in *Proceedings of the 14th International Particle Accelerator Conference, Venice, Italy* (JACoW, Geneva, Switzerland, 2023), pp. 2781–2784.

[8] A. Bellandi, W. Hillert, and J. Branlard, LLRF control techniques for the European XFEL continuous wave

upgrade, Ph.D. thesis, Universität Hamburg, 2021, PUBDB-2022-00857.

[9] J. Holzbauer, B. Chase, L. Doolittle, J. Einstein-Curtis, Y. Pischalnikov, W. Schappert, and C. Serrano, Active microphonics compensation for LCLS-II, in *Proceedings of the 9th International Particle Accelerator Conference, IPAC-2018, Vancouver, BC, Canada* (JACOW, Geneva, Switzerland, 2018), pp. 2687–2689.

[10] R. Rybaniec, V. Ayvazyan, J. Branlard, S. P. Butkowski, H. Schlarb, C. Schmidt, G. W. Cichalewski, and K. Przygoda, Real-time estimation of superconducting cavities parameters, in *Proceedings of the 5th International Particle Accelerator Conference, IPAC-2014, Dresden, Germany* (EPS-AG, Dresden, 2014), pp. 2456–2458.

[11] A. Bellandi, Ł. Butkowski, B. Dursun, A. Eichler, Ç. Gümüş, M. Kuntzsch, A. Nawaz, S. Pfeiffer, H. Schlarb, C. Schmidt *et al.*, Online detuning computation and quench detection for superconducting resonators, IEEE Trans. Nucl. Sci. **68**, 385 (2021).

[12] V. Ziemann, Simulations of real-time system identification for superconducting cavities with a recursive least-squares algorithm, Phys. Rev. Accel. Beams **26**, 112003 (2023).

[13] D. G. Luenberger, Observing the state of a linear system, IEEE Trans. Mil. Electron. **8**, 74 (1964).

[14] D. Luenberger, Observers for multivariable systems, IEEE Trans. Autom. Control **11**, 190 (1966).

[15] A. Gelb, *Applied Optimal Estimation* (The MIT Press, Cambridge, MA, 1974).

[16] E. Wan and R. Van Der Merwe, The unscented Kalman filter for nonlinear estimation, in *Proceedings of the IEEE 2000 Adaptive Systems for Signal Processing, Communications, and Control Symposium, Lake Louise, AB, Canada* (IEEE, New York, 2000), pp. 153–158.

[17] T. Schilcher. Vector sum control of pulsed accelerating fields in Lorentz forces detuned superconducting cavities, Ph.D. thesis, Universität Hamburg, 1998, PUBDB-2015-05496.

[18] G. J. Balas, Linear, parameter-varying control and its application to a turbofan engine, Int. J. Robust Nonlinear Control **12**, 763 (2002).

[19] F. Marhauser, Method for *in situ* and in operando cavity loaded q extraction in superconducting rf accelerators, Phys. Rev. Accel. Beams **24**, 032001 (2021).

[20] B. Richter, A. Bellandi, J. Branlard, and A. Eichler, Code for paper "Estimation of superconducting cavity bandwidth and detuning using a Luenberger observer", https://github.com/richtbz/srf_luenberger (2026).

[21] B. Richter, A. Bellandi, J. Branlard, and A. Eichler, Dataset for paper "Estimation of superconducting cavity bandwidth and detuning using a Luenberger observer", 10.5281/zenodo.18292997 (2026).

[22] A. Bellandi, J. Branlard, M. Diomede, M. Herrmann, S. Pfeiffer, and C. Schmidt, Calibration of superconducting radio-frequency cavity forward and reflected channels based on stored energy dynamics, Nucl. Instrum. Methods Phys. Res., Sect. A **1069**, 169825 (2024).

[23] A. Brandt, Development of a finite state machine for the automated operation of the LLRF control at FLASH, Ph.D. thesis, Universität Hamburg, 2007, PHPPUBDB-5819.